Chapter 7

Boundary Layer Processes and Land Surface Interactions on the Mesoscale

R.A. Pielke, Sr.[1], G. Dalu[1,2], J. Eastman[1], P.L. Vidale[1], and X. Zeng[3]

[1] *Colorado State University, Department of Atmospheric Science, Fort Collins, USA.*
[2] *Institute for Atmospheric Physics IFA-CNR, Rome, Italy*
[3] *Department of Atmospheric Science, University of Arizona, Tucson, USA.*

Abstract

Analytic, numerical modeling and observational comparisons are presented which indicate that flat but heterogeneous landscapes result in spatially variable convective boundary layer structure (CBL). This variable CBL can result in significant mesoscale circulations when the large-scale wind is relatively weak and the landscape heterogeneities are sufficiently large. When cumulus cloud development occurs, the smaller-scale heterogeneities become more important, relative to the clear sky situations.

1   Introduction

Mesoscale atmospheric systems have spatial and temporal structures that have a wind field which is not in near-balance with the mass field, even in the absence of turbulent momentum exchange. In addition, the temperature field accurately describes the mass field (i.e., the pressure field is in near hydrostatic balance; Pielke, 1984).

There are two basic types of mesoscale systems – those that develop within the atmosphere and those which are generated by surface forcings. In our paper, we focus on the second type of mesoscale systems over flat terrain. These mesoscale systems, which are surface-forced, necessarily are strongly influenced by boundary layer processes.

There has been considerable study of boundary layer – mesoscale interactions, particularly for clear sky conditions, but also when cumulus clouds occur (see Mahrt et al. (1994), Avissar et al. (1995) and Dalu et al. (1996) for recent summaries). There is also a recent compilation of work on these topics in the AMS Preprint Volume of the Symposium on the Boundary Layers and Turbulence (Land-Surface) held 2 – 7 February 1997 in Long Beach. While there is considerable evidence, as summarized in these papers, that mesoscale effects are important over heterogeneous landscapes, this conclusion has not been universally accepted. Indeed, as an example, Doran et al. (1997) presents a thought-provoking paper where he shows that when real-world data is used, mesoscale fluxes in clear sky conditions from landscape heterogeneity are relatively unimportant. This paper is important in that it has helped focus a critical remaining research question.

In our paper, Section 2 offers an analytical analysis of the influence of landscape heterogeneity on boundary layer and mesoscale processes. Sections 3 and 4 provides model results, and some observational comparison, for the BOREAS and FIFE field experiments. Section 5 discusses procedures to represent mesoscale fluxes due to landscape variability in flat terrain.

2 Analytic studies

If we assume, as originally discussed in Dalu et al. (1996), that a diabatic heat flux, Φ, is sinusoidally periodic with k as a wavenumber and L_m as a wavelength, and that it linearly decreases with height up to h where it vanishes; then we have within the CBL for $0 < z < h$:

$$\Phi = \Phi_0 \, q(t) \, (h - z) \, He(h - z) \left[\frac{1}{2} + \frac{1}{2} \sin(kx) \right] ; \tag{1}$$

$$m = \frac{2R_0}{L_m} \qquad ; \qquad k = \frac{m\pi}{R_0} = \frac{2\pi}{L_m} \; .$$

Here He is the Heaviside step function. This situation could correspond to inland patches of periodically heated land, such as regions of landscape variability; m is the number of patches of L_m wavelength per Rossby radius R_0. In fact, once the mesoscale response to sinusoidal forcing is known, more general configurations can be investigated through the use of the Fourier transform and inverse transform. The relation between the buoyancy source, Q, and the diabatic heat flux, Φ, is:

$$-\frac{g}{\rho \, c_p \overline{\overline{\Theta}}} \frac{\partial \, \Phi(x, z, t)}{\partial z} = Q_0 \, q(t) \, He \, (h - z) \left[\frac{1}{2} + \frac{1}{2} \, \sin(kx) \right] \; . \tag{2}$$

Because of advection and diffusion, the depth of the CBL is governed by:

$$\left(\frac{\partial}{\partial t} + \lambda\right) h + U\,\frac{\partial h}{\partial x} = \frac{2\,Q_0\,q(t)}{N_0^2}\,\left[\frac{1}{2} + \frac{1}{2}\,\sin\,(kx)\right] + K\,\frac{\partial^2 h}{\partial x^2}\,, \qquad (3)$$

where λ is the Rayleigh friction (Dalu et al., 1996). Through a Laplace transform, this equation can be reduced to:

$$\left[-K\,\frac{\partial^2}{\partial x^2} + U\,\frac{\partial}{\partial x} + p\right] h = \frac{2\,Q_0\,q(s)}{N_0^2}\,\left[\frac{1}{2} + \frac{1}{2}\,\sin\,(kx)\right]; \quad q(s) = \frac{1}{s}. \qquad (4)$$

U is the large-scale flow, k the diffusion coefficient, and N_0 is the Brunt-Väisäla frequency. Here s is the Laplace transform of time t (Fodor, 1965), and $p = s + \lambda$.

Since the boundary conditions are periodic, Eq. (4) has the following solution:

$$h = \frac{Q_0}{spN_0^2}[1 + a_1 \sin(kx) + a_2 \cos(kx)] = \frac{Q_0}{spN_0^2}[1 + a \sin(kx + \vartheta)]; \qquad (5)$$

$$a_1 = \frac{p(p + Kk^2)}{(p + Kk^2)^2 + k^2U^2}; \qquad a_2 = -\frac{pkU}{(p + Kk^2)^2 + k^2U^2}; \qquad (6)$$

$$\lim_{k,U\to\infty} a_1,\ a_2 = 0;$$

$$a = p\left[(p + Kk^2)^2 + k^2U^2\right]^{-\frac{1}{2}}; \qquad \vartheta = -\tan^{-1}\left(\frac{kU}{p + Kk^2}\right). \qquad (7)$$

Asymptotically, when $t \gg \lambda^{-1}$ using the inverse Laplace transform,

$$h(t) = \lim_{s\to 0} sh(s) = \frac{Q_0}{\lambda N_0^2}\left[1 + a \sin\,(kx + \vartheta)\right]. \qquad (8)$$

When the time, t, is sufficiently larger than the dissipation time, λ^{-1}, then $p \approx \lambda$ in Eq. (5) to (7), and the mesoscale circulation reaches its maturity. The depth of the CBL for this situation is given by

$$h = h_0\frac{1}{2}\left[1 + a_1 \sin(kx) + a_2 \cos(kx)\right] = h_0\frac{1}{2}\left[1 + a\,\sin(kx + \vartheta)\right]\ ; \qquad (9)$$

$$\text{where } h_0 = \frac{2Q_0}{\lambda N_0^2}\,,$$

with the following limit value of the parameters

$$\lim_{t \to \infty} p = \lambda; \quad \lim_{k,U \to \infty} a = 0; \quad \lim_{k \to 0,\infty} \vartheta = 0; \quad \lim_{U \to \infty} \vartheta = -\frac{\pi}{2}; \quad \lim_{U \to 0} \vartheta = 0 \ . \quad (10)$$

From Eq. (10), the maximum depth of the CBL, h_a is:

$$h_a = \frac{1}{2} h_0 (1 + a) \quad ; \quad \lim_{k,U \to \infty} h_a = \frac{h_0}{2} \ , \quad (11)$$

where h_a, as a function of the wavenumber k, is shown in Fig. 1.

The amplitude of the sinusoidal modulation of the height of the CBL, a, decays as $1/(kU)$ for strong ambient flow, and as $1/Kk^2$ because of diffusion at large wavenumbers. The phase shift, ϑ between the modulation of the CBL and the diabatic forcing increases as $k\,U$ for strong ambient flow. The large-scale advection is more effective at large wavenumbers; the modulation of the CBL can become out-of-phase with the diabatic forcing, in fact, when $U \neq 0$ and $k \approx 1$ [km]$^{-1}$, $\vartheta \approx -\pi/2$. However, asymptotically, when the synoptic advection kU or the diffusion Kk^2 are large, the CBL becomes almost horizontally uniform with a depth equal to half of its maximum depth reached in the absence of advection or diffusion.

Nonlinear model simulations have shown that nonhomogeneities of size 450 - 900 m do not change the development of the convective boundary layer (Hechtel et al., 1990). In other words, when either the advection time, $(kU)^{-1}$, or the diffusion time, $(Kk^2)^{-1}$, become much smaller than the characteristic time scale, T, the intensity of the local flow becomes negligible because of the weakening of the mesoscale available potential energy (see Fig. 2). Mesoscale available potential energy ($MAPE$) is directly related to the magnitude of the horizontal gradient of boundary layer heating, and the depth over which it is present.

$$MAPE = \int_{-R_0}^{R_0} dx \int_0^h dz \left(\frac{g\,z\,\theta_i}{\Theta} \right) - \int_{-R_0}^{R_0} dx \int_0^{h_0/2} dz \left(\frac{g\,z\,\theta_f}{\Theta} \right) =$$
$$\frac{g\,\Theta_z}{\Theta} \frac{h_0^3}{24} 3a^2 \left[R_0 - \frac{1}{2k} \sin(2k\,R_0) \right] \ , \quad (12)$$

where θ_i is the initial potential temperature perturbation, and θ_f is the final potential temperature perturbation, which minimizes the potential energy (Dalu and Green, 1980).

When the synoptic wind is sufficiently strong, the vertical wave number squared becomes negative; then the mesoscale perturbation is in the form of propagating waves which feed directly on the ambient flow while the conversion of mesoscale potential energy into mesoscale kinetic energy is negligible.
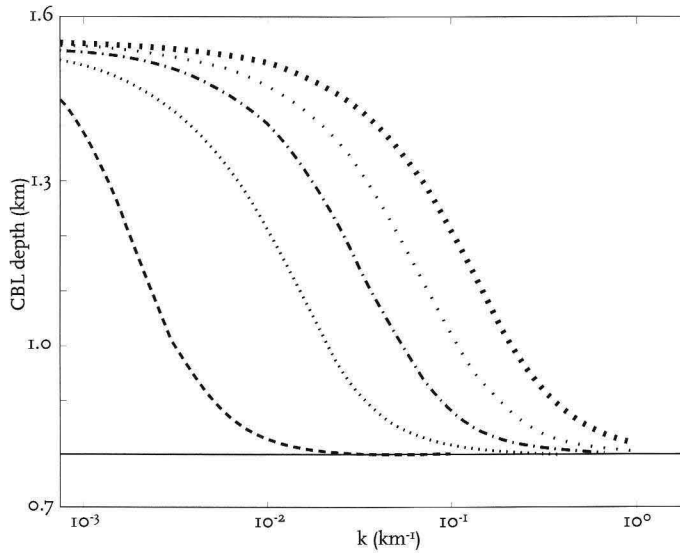
Fig. 1. Maximum depth of the CBL, h_a, as a function of horizontal wavenumber, wind intensity, and diffusion for U = 0 and K = 0 (solid line); U = 0, 1, 2.5, 5, 10 m s^{-1} and K = 100 m s^{-2}. The upper curve refers to the lowest wind intensities. Wind intensity increases from the upper to the lower curve. A wind of U = 10 m s^{-1} blends inhomogeneities in the CBL of 50 km or smaller. U= 5 m s^{-1} blends inhomogeneities of 5 km or smaller. U = 1 m s^{-1} blends inhomogeneities of 1 km or smaller (from Dalu et al., 1996).
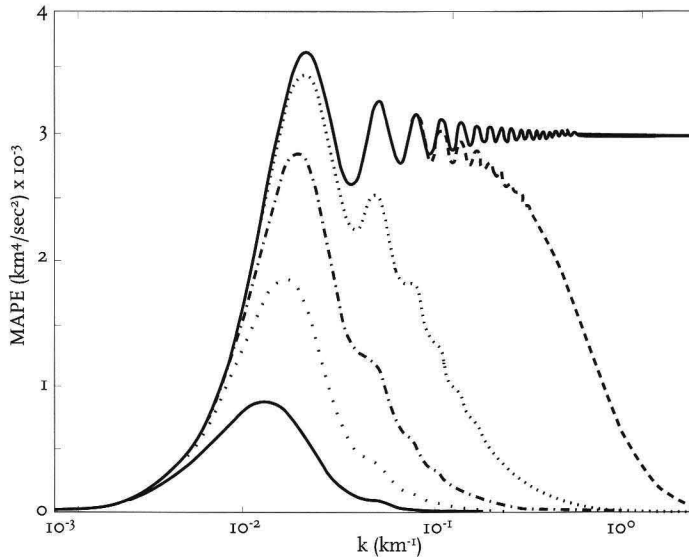

Fig. 2. The Mesoscale Available Potential Energy, MAPE as function of wavenumber k. Here MAPE becomes negligible over horizontal inhomogeneities of 50 km or smaller when U = 10 m s^{-1}; 5 km or smaller when U = 5 m s^{-1}; 1 km or smaller when U = 1 m s^{-1}. The upper curve refers to the lowest wind intensity. Wind intensity increases from the upper to the lower curve (from Dalu et al., 1996).

159

3   Heterogeneous landscape and convective boundary layers

The BOREAS project covered a regional scale (approximately 10^6 km^2), over very heterogeneous terrain and land cover. Figures 3a and 3b were produced using a land cover classification derived from NOAA Advanced Very High Resolution Radiometer (AVHRR) data (Steyaert et al. 1997). Figure 3a covers most of the BOREAS domain; Fig. 3b is a subset of 3a, corresponding to the white rectangle in Fig. 3a. The atmospheric model RAMS is used to simulate the observations.

The RAMS grid number 1, corresponding to the domain of Fig. 3a, comprised both the Northern Study Area (NSA) and the Southern Study Area (SSA), approximately covering the region from 52.09 to 56.60 degrees north and 107.63 to 96.38 degrees west (about 700 by 500 km), with a horizontal grid separation of 10 km. Grid 2 covered most of the SSA (the domain of Figure 3b), from 53.42 to 54.29 degrees north and 106.03 to 104.55 degrees west (about 95 by 95 km), with a horizontal grid increment of 2.5 km. Grid 3 (the white box at the left hand side in Figure 3b) was designed to cover the region around Candle Lake, for comparison with aircraft observations, and comprised the region from 53.72 to 53.96 degrees north and 105.49 to 105.19 degrees west (about 24 by 26 km), with a grid separation of 625 m (which provides an effective horizontal resolution of 2.5 km).

The vertical grid increment was initiated at 30 m above ground level (so that the first atmospheric level corresponded as nearly as possible to that of most aircraft measurements) and was then telescoped upwards through 28 levels, with the model top at 12000 m on average, depending on the surface terrain. All three grids utilize an ensemble-based parameterization for turbulence (a Smagorinsky form in the horizontal and a Richardson-based form in the vertical; see Lüpkes and Schlünzen , 1996, and also Vidale et al., 1997). An ensemble-based form was used since even the fine grid has a resolution coarse enough such that none of the turbulence is explicitly resolved (the boundary layer depth on the simulated date reached about 2 km).

Within the study region (Fig. 3a) there are numerous lakes (13% of the coverage by area), variable topography, several forest types and large areas of burned vegetation in various stages of regeneration. A number of surface, airborne, and satellite measuring efforts (e.g. surface energy balance and biophysical characteristics) took place during BOREAS (Figs. 3 and 5 in Sellers et al., 1995), providing good opportunities to evaluate if and when mesoscale circulations can become an important atmospheric feature in this region.

The Surface-Atmosphere Vegetation Transfer Scheme (SVATS) used in RAMS is the LEAF-2 sub-model (Lee, 1992; Walko et al., 1998) , which is a one-level canopy model capable of representing the surface energy balance as mediated by surface aerodynamics (Louis et al., 1982) , parameterized canopy conductance (Jarvis, 1976) , and multi-level dynamic soil processes (Tremback et al., 1985) . Within each LEAF-2 grid cell, a number of surface cover patches
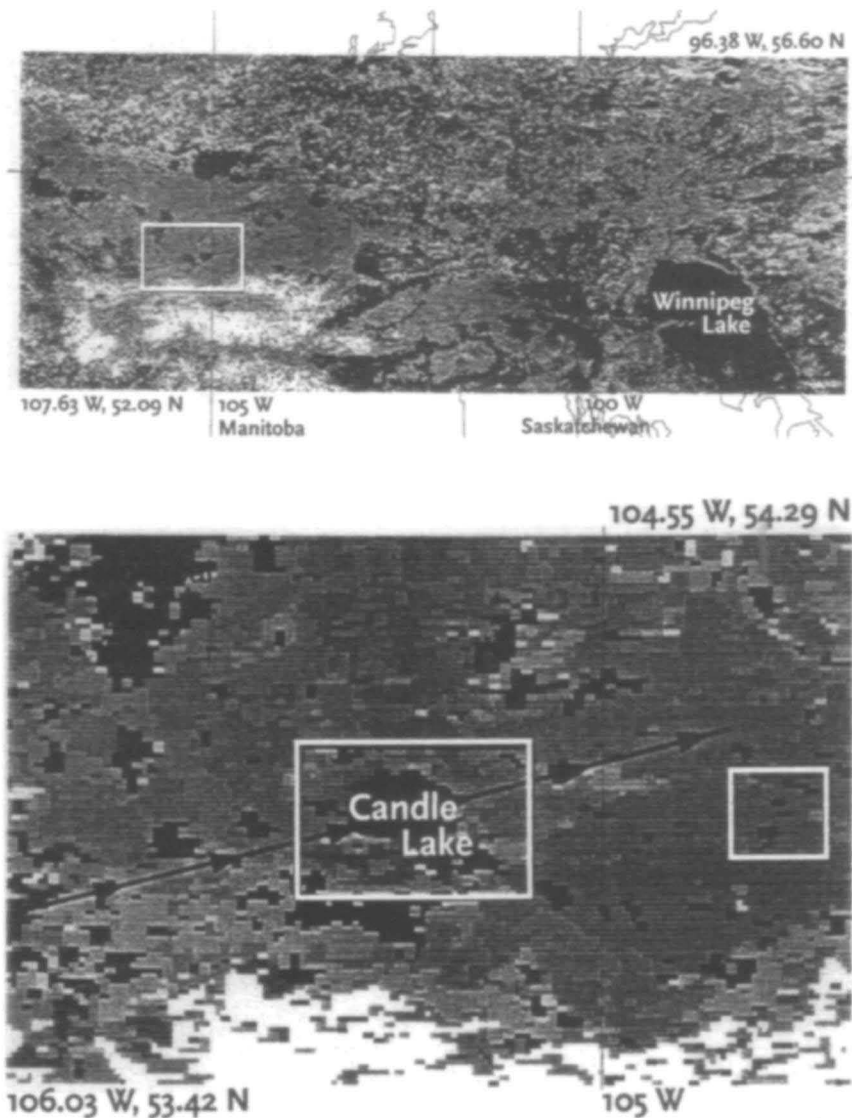
Fig. 3. a (top): The AVHRR 1 km BOREAS regional land cover classification. Dark lines and letters indicate latitudes and longitudes with an interval of 5 degrees. The map corresponds to RAMS Grid 1 (52.09 to 56.60 degrees north and 107.6 to 96.38 degrees west); Fig 3b (bottom): Subset of Fig. 3a, corresponding with the white rectangle in Fig 3a. The AVHRR 1 km BOREAS regional land cover classification for RAMS grid number 2. Dark lines indicate latitudes and longitudes in degrees with an interval of 0.5 degrees. The map limits are 53.42 to 54.29 degrees north and 106.0 to 104.6 degrees west. The white box at the right handside corresponds to the Twin Otter integrated flux region. The white box at the left handside represents grid box 3 around Candle Lake. Other symbols are explained in the text.

co-exist, with a minimum number of two (one water body and one vegetation type) and a maximum number limited by computer resources. Quantities which are averaged linearly by patch fractional area are the actual surface fluxes, and not the patch biophysical characteristics, in agreement with the discussion of Sun and Mahrt (1995) and Mahrt et al. (1997) on the computation of fractional contributions to surface fluxes. The technique used to separate mesoscale and turbulent quantities for our study was based on the one described by Mahrt et al. (1994). In the model, this translated into calculating domain averages over about one local Rossby radius by layer, and deviations from this average at each grid point. Correlations of these resolved perturbations were then used to compute resolved fluxes.

3.1 Surface boundary conditions and initialization

The surface vegetation characteristics are defined using the AVHRR vegetation classification (Fig. 3a) which has nominal resolution at 1 km, and actual useful resolution at 2-3 km. Grid 3 is designed, therefore, to be able to resolve the finest scales defined by this product; Grids 1 and 2 were initialized, for separate model runs, by the use of a predominant pixel or by a mosaic (Avissar and Pielke, 1989) technique. Other surface boundary conditions included 1 km Digital Elevation Maps (DEMs), surface water bodies (defined by the AVHRR product) and soil type distribution, which are interpolated to each grid.

The initial meteorological conditions and the hourly grid 1 boundary conditions (outer five points) are derived from the United States ETA model analysis (Black, 1994) at 00 and 12 UTC, using the Davies (1983) technique. Surface water temperature is defined using aircraft measurements (Sun et al., 1997) . Extensive use of the BORIS (BOREAS Information Service) data sets allowed us to refine the model initialization locally with all available information from observations, especially in the case of soils data (e.g. profiles of initial soil water content and soil temperature, which were locally distributed according to vegetation type). After doing this, the model was allowed to run for more than a full diurnal cycle (two nights and one day) before using its output for analysis. This was to permit the soil heat and moisture component of the model to adjust to the atmospheric forcing.

The day of 4 July 1994 is selected because of its relevance to the rest of the BOREAS community; it presented very clear skies, and was ideal for radiative transfer work. The synoptic scale winds in this case study are not weak, reaching 10 m s^{-1} at the surface during the day and over 11 m s^{-1} during the night, so this was certainly not an ideal case for mesoscale circulations (Dalu et al., 1996; Wang et al., 1997) . The 21 July 1994 case was simulated by initializing the model on 20 July at 00 UTC (19 July, 18.00 Local Time) and running RAMS for 60 hours, as mentioned above. The temperature of the

Candle Lake water (and of every other lake in the domain) for 20-22 July 1994 was set at 283 K. Soil temperature and moisture profiles were initialized using information from the Automated Meteorological Stations (AMS) and the Atmospheric Environmental Services (AES) network on 20 July.

3.2 Observational and model evaluation of mesoscale fluxes

Flux aircraft measurements at various heights (for instance, 30 m for the NOAA LongEZ, 100 m and more for the NCAR Electra) offered additional evidence of the very heterogeneous horizontal distribution of surface fluxes of heat, moisture, momentum and CO_2, calculated by eddy correlation techniques. Transects over the Candle Lake region in the SSA comprised regions predominantly covered by deciduous trees (aspen) in the west, transitioning into a mixed forest cover and, proceeding eastward, into a wet conifer region (Black Spruce, Jack Pine, fens, bogs, etc.). Special model slices through grids 2 and 3 were generated, corresponding to aircraft transects. Figure 4 (data here reproduced with permission of Crawford and Baldocchi) shows temporally averaged sensible and latent turbulent fluxes, measured by the NOAA LongEZ aircraft over 13 legs between 15.32 and 23.20 UTC on 21 July 1994 (transect indicated on Fig. 3b).

In particular, the LongEZ measurements of sensible heat over Candle Lake for 21 July 1994, showed a sharp reduction from about 275 W m^{-2} to almost -25 W m^{-2} when moving from the forested regions around the lake to a position directly over the lake. The magnitude of the fluxes and their horizontal gradients over this transect were found to be very similar to others measured during July 1994 by the LongEZ aircraft, and not an example of a single occurrence. Figure 4 also shows the turbulent fluxes modeled by RAMS, temporally averaged through the same period. The model was capable of capturing the spatial pattern of the fluxes quite accurately. The magnitudes of the fluxes were also in reasonable agreement, even without any special tuning of the model parameters that control canopy conductance. For the correct interpretation of the comparison between the two data sets, it is important to remember that the model fluxes are representative of a set of volume averages over grid cells corresponding to the aircraft transect, while the aircraft fluxes are transect and time averages.

Referring to Fig. 3b, the land cover to the southwest has contributions from the deciduous forest and disturbance classes (higher albedo, lower LAI), while the land to the northeast displays lower albedo (conifers) and some patches of drier soils (for the uphill dry conifer). The modeled gradient was not as finely resolved as the measured one, but it is clear from the plot that the horizontally integrated heat input from the surface east of the lake was higher than that from west of the lake. The modeled sensible heat flux (maximum of 265 W m^{-2}) was on average about 50 W m^{-2} higher than the observations,
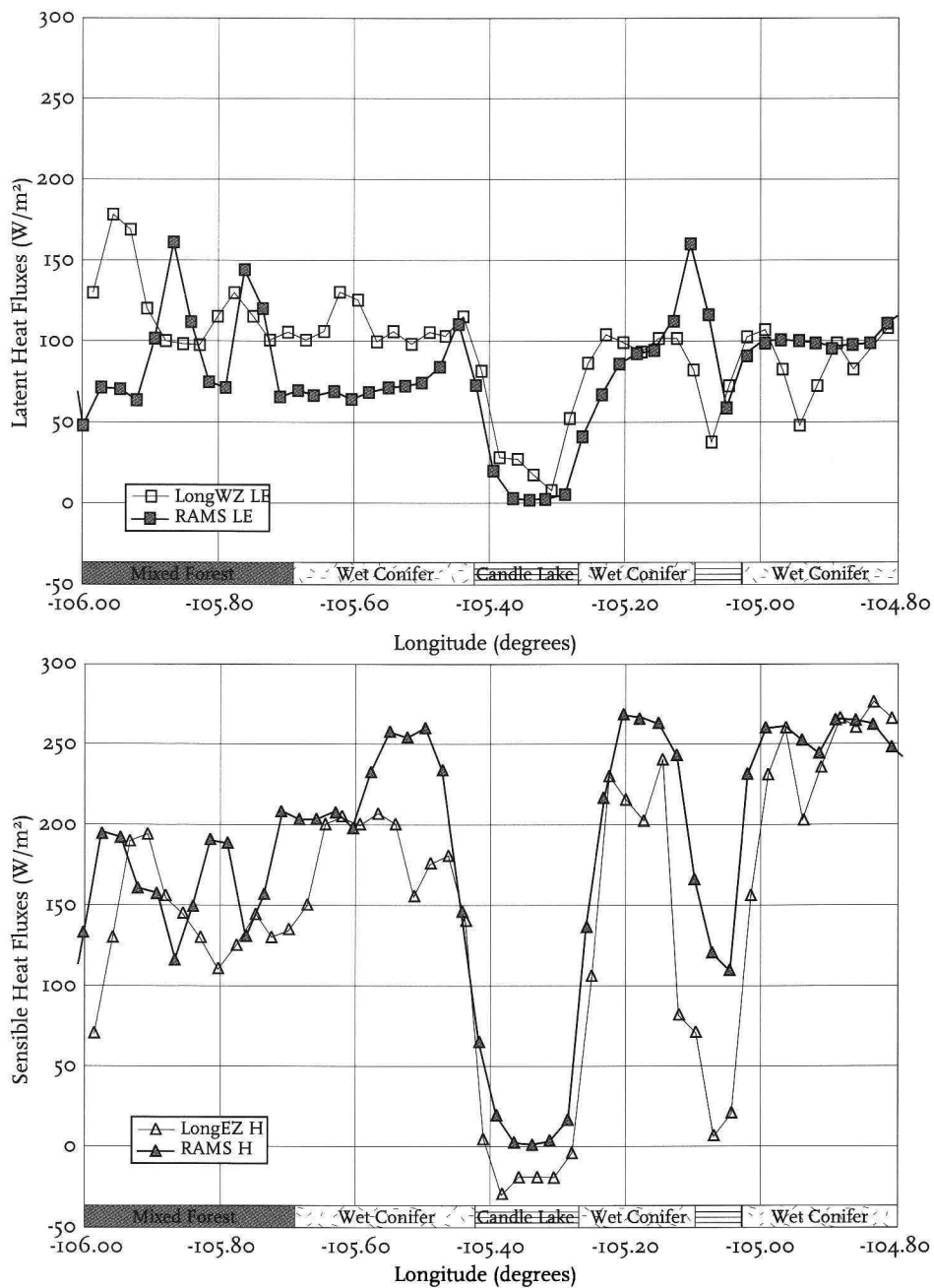
163

Fig. 4. RAMS and NOAA LongEZ (provided by Crawford and Baldocchi) transect surface turbulent fluxes (W m^{-2}) for the SSA, averaged between 15 and 23 UTC, 21 July 1994. Sensible heat fluxes are labeled as H, latent heat fluxes are labeled as LE. Predominant surface vegetation types, as interpreted from aircraft data, are indicated along the transect.

especially on the west side of the lake, while the latent heat flux was about 50 W m^{-2} lower on average than the observed one. The spatial pattern in the modeled latent heat fluxes show slightly higher values to the west of the lake than to its east, again in agreement with measurements.

Previous sensitivity tests suggested that the main controlling parameter for the surface fluxes calculated in the present version of LEAF-2 is the Leaf Area Index (LAI). LAI was here indirectly specified (with a Look Up Table (LUT) approach) by the land cover classification, and not linked to remote sensing, so that the modeled spatial gradients in vegetation parameters are only representative at scales larger than actually occur along this transect (i.e., the aircraft, of course, measured fluxes from all patch sizes in the flight cross-sections, while the model used patch data that was limited to 2-3 km of effective resolution). The horizontally homogeneous sensible heat flux plateaus over the mixed forest class on the west portion of the graph are also indicative of how the LUT approach is not capable of representing intra-class heterogeneity of biophysical parameters.

The important point for the modeling results described below is that the gradient between Candle Lake and its surrounding measured (at its peak time) over 300 W m^{-2} over about 20 km, (thus a scale comparable to the local Rossby radius; see Section 2) and, according to linear theory, was sufficient to force a mesoscale circulation under the proper synoptic conditions. For maximum effect to occur, linear theory suggests that the two coastal breeze cells should constructively interact at the lake center to form a maximum subsidence and surface divergence pattern, lagging by about two hours the time of maximum diurnal heating (Dalu et al., 1996).

Occurrences of a lake breeze over Candle Lake were also successfully simulated with our atmospheric model for some calm wind days in June (IFC1) and July (IFC2) 1994 and their divergence/convergence patterns agreed well with the analysis of (Sun et al., 1997), which was conducted for Candle Lake during similarly calm days. The contrast could also be seen in the temperature gradient over the same transect for the summer season (Figs. 2a and b in Sun et al., 1997). On 21 July 1994, the date of our model simulation in this paper, the diurnal evolution of the horizontal wind divergence over the center of Candle Lake, derived from data of the LongEZ aircraft (Fig. 5), appeared as a clear lake breeze signature. The timing of the divergence pattern reflects both the two hour lag mentioned earlier in this subsection and the fact that the breeze cell was displaced to the northeast. The mass divergence measured about 0.0002 s^{-1} during the heating period, between 13.00 and 17.00 local time (19 and 23 UTC), while a convergence (negative divergence, with peak of -0.0005 s^{-1}) was still present between 9 and 12 local time, at the end of the nocturnal cooling period.

Following the discussion above, turbulent surface sensible heat fluxes were quite pronounced over the grid 2 region ($\Delta x = 2500$ m). This could be explained by the large LAI of dense conifer, but also to horizontal advection of cooler air due to a mesoscale circulation caused by differential heating between
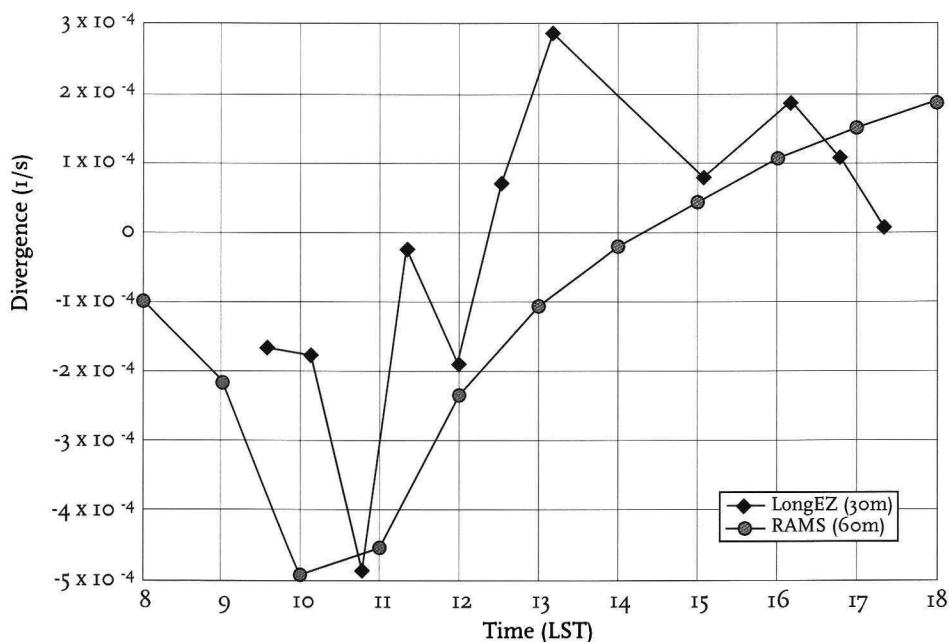
Fig. 5. Wind divergence (1/s) over the center of Candle Lake on 21 July 1994 between 8 and 18 LST, as calculated from wind measurements of the NOAA LongEZ at 30 m (data provided by J. Sun), and RAMS 60 m divergence (1/s) at corresponding times and locations within grid 3.

the sloping terrain and the local depression where Candle Lake is located. The lowest sensible heat fluxes are found to correspond to the positions of Candle Lake (center) and Montreal Lake to the northwest.

Mesoscale (resolved) fluxes over grid 2 (with contributions from grid 3, through the two-way nesting), calculated from the correlations of domain average residuals of temperature and vertical velocity (for sensible heat), displayed maxima at higher levels, in the upper portion of the BL. Their depth was typically confined to a layer of about 2000 m. The first substantial mesoscale sensible heat flux (small patches with maxima up to 270 W m^{-2}) was produced by the model at 22 UTC 21 July 1994 (depicted in Fig. 6) and its magnitude oscillated, until another maximum (180 W m^{-2}) of similar vertical distribution was realized at 04 UTC on 22 July. The heating at 22 UTC seemed to be associated with a fossil (remaining part of diurnal solenoid over the forming nocturnal layer) uphill flow over the northern portion of Candle Lake and the NE slope. The heating at 04 UTC appears to be associated with the downward export of colder air (from the nocturnal residual layer), over the local orography minima and over Montreal Lake, where drainage flow and surface divergence occurred. The mesoscale latent heat flux (not shown) had a maximum around 22 UTC and a shorter life time. Most fields displayed southwest to northeast banding, which was a signature of the predominant southwesterly flow superposed on the local circulations caused by the orography.
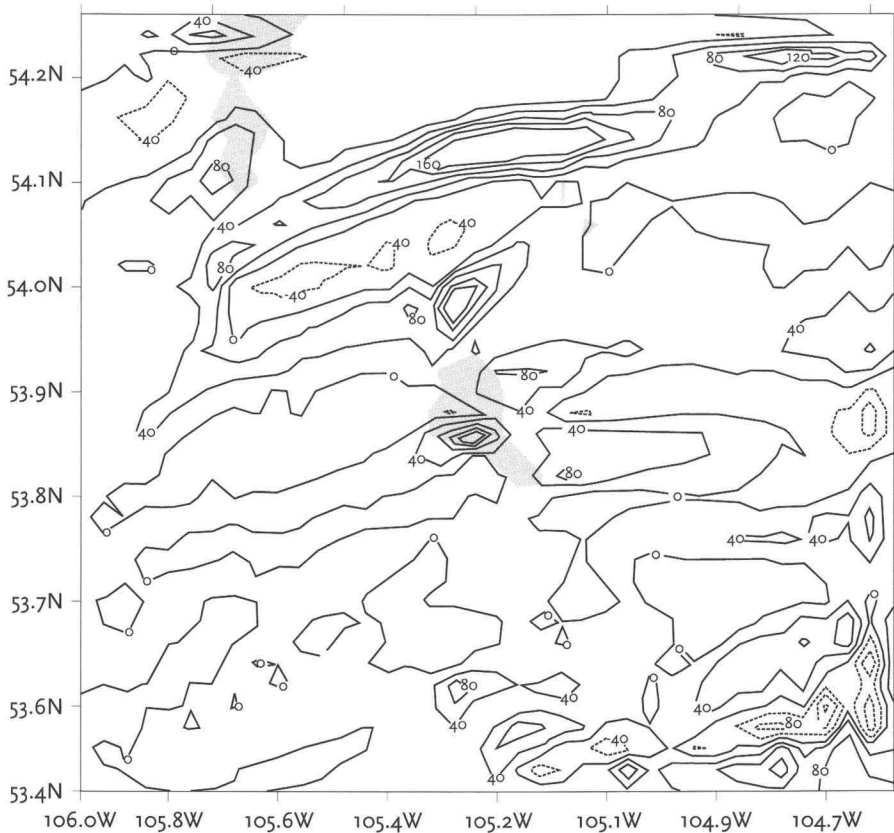
166

Fig. 6. Fine-grid run: mesoscale (resolved) sensible heat flux (W m^{-2}) for grid 2, 22 UTC, 21 July 1994 at 1200 m. Contour interval of 20 W m^{-2}. Reference lines are in decimal degrees.

By visually inspecting the grid 2 domain over many time periods, we found that the resolved fluxes contributed positively to the horizontally integrated heat budget of each model level over many hours and were observed to be horizontally displaced by the main flow. Vertically, we found these fluxes to be present exclusively within twice the depth of the diurnal CBL. The magnitude of these fluxes for this case was indeed smaller than the magnitude of the surface turbulent fluxes, but their vertical distribution differed in that they peaked at higher levels, unlike the turbulent flux influence, which decays with height.

In terms of time scales, the mesoscale fluxes peaked about three hours after the realization of the maximum turbulent fluxes (19 UTC), so that their phase lag was comparable with the time scale predicted by linear theory in Section 2. Significant sensible heat fluxes persisted from 18 UTC to about 08 UTC between 21 and 22 July 1994.

Grid 3 ($\Delta x = 625$ m) was spawned around Candle Lake with the purpose of resolving possible lake-induced circulations. After one full diurnal cycle, the model developed a well defined lake breeze, with a subsiding cell (-0.286 m/s)

to the NW of the lake center and maximum ascending motion (0.157 m/s) at the north-west bank of the lake. The downward motion region revealed a shape and position that confirmed the influence of Candle Lake. The positive vertical velocity regions were distributed over the land around the lake, although shifted by the southwesterly winds.

A lake-induced circulation was also observed at night, with ascending motion (0.115 m/s) over the eastern part of the lake and descending motion (as large as -0.104 m/s) over the western lake boundaries. Most of the ascending motion over the central part of the lake was shifted eastward by the prevailing winds.

This pattern of ascending/descending motion corresponds to a diurnal cycle in mass divergence over the lake. This pattern was observed on 21 July by three aircraft, as discussed in Section 3.2, and is portrayed in Fig. 5. During the diurnal heating period, with ascending motion over the lake boundaries and descending motion over the center of the lake, there was divergence at low levels near the lake center. During the nocturnal cooling period, there was descending motion over the lake boundaries and ascending motion at low levels near the lake center, where the land breeze converged with the prevailing flow. A typical conceptual model for the Candle Lake circulation was also given by Sun et al. (1997), in their Fig. 3, which is consistent with our modeling results. Additional detail on this study is reported in Vidale et al. (1997).

4   Heterogeneous landscape and cumulus convection

In this section we explore the effects of landscape patchiness and shallow cumulus clouds on the surface energy budget. The area studied is the First International Satellite Land Surface Climatology Project Field Experiment (FIFE) study area in Kansas (Sellers et al., 1992). The experiment involves four LES integrations employing the RAMS model. The study is designed to assess the possibility that a linear relationship can be used to sum up the contributions of each patch within an area to obtain the surface energy budget for the entire area (Sellers et al., 1992). In addition, we will examine the effects of moist processes and their importance to boundary layer development by using the explicit modeling of cumulus clouds available in RAMS.

In each simulation a fine mesh, with a Δx of 200 m, was contained within a mesh with a Δx of 800 m, which was embedded within a mesh with 3.2 km horizontal increments. The vertical grid increment was 200 m on all grids, up 5 km. The finest mesh covered the entire FIFE study area. All simulations were initialized using a climatological sounding for the area. In all integrations the coarse grid was first run by itself for 3 hours, starting at 12 GMT, after which all grids were integrated forward for a total model integration time of 8 hours.

The control run employ homogeneous vegetation and no cumulus clouds. A second run used variable vegetation with no cumulus clouds. The third simulation had homogeneous vegetation and cumulus clouds were permitted to develop, while the fourth integration used variable vegetation and cumulus clouds were permitted.

A factor separation method, discussed in Stein and Alpert (1993) was applied to examine the relative contribution of cumulus clouds and heterogeneity on the latent and sensible heat fluxes from the surface to a height of 2.7 km. The method allows one to obtain the contribution of a given factor to any predicted field. In many previous studies of the impact of 2 variables on predicted fields, only 3 simulations have usually been conducted. However, this fails to address the contribution due to the interaction of 2 variables. In our FIFE study a fourth simulation with both (variable vegetation and cumulus clouds) variables active was performed. For a complete discussion of the methodology see Stein and Alpert (1993).

The control experiment exhibits structure common to previous horizontally homogeneous LES simulations[1]. The cellular nature of the maximums and minimums are well pronounced and interspersed throughout the domain. In contrast, the model run with variable vegetation alone produces large increases in the magnitude of the latent heat flux over areas where cropland/mixed farming are present. The opposite is true for the surface sensible heat fluxes.

The domain-averaged surface sensible and latent heat fluxes are shown in Figure 7. The control experiment describes most of the temporal variability, with the sensible and latent heat fluxes out of phase, as the transpiration shuts off later in the afternoon. The time series of the domain-averaged latent heat fluxes at 1100 m is shown in Figure 8. At this height the sensible heat fluxes (not shown) are small with the cumulus cloud only simulation generally showing the largest contribution. The latent heat shows a large variability. This height is near the top of the boundary layer where significant cumulus cloud development occurs. The contribution of the clouds is evident nearly an hour before any of the other curves exhibit an appreciable magnitude. This is due to the added buoyant effect when cumulus clouds occur. Also, note that the effect due to the interaction of cumulus clouds and variable vegetation is significant, while the variable vegetation alone contributes little to the fluxes at this level.

In summary, there are larger contributions to sensible and latent fluxes when cumulus clouds are permitted to develop and when heterogeneous landscapes are present. This is due to the added buoyancy effects from the latent heat release associated with water phase changes, which is modulated in its strength and location when variable landscapes are present. Domain averages also indicate, however, that the contribution to sensible and latent fluxes due

---

[1] A color figure of the surface sensible and latent heat fluxes for the different experiments is available from the lead author.
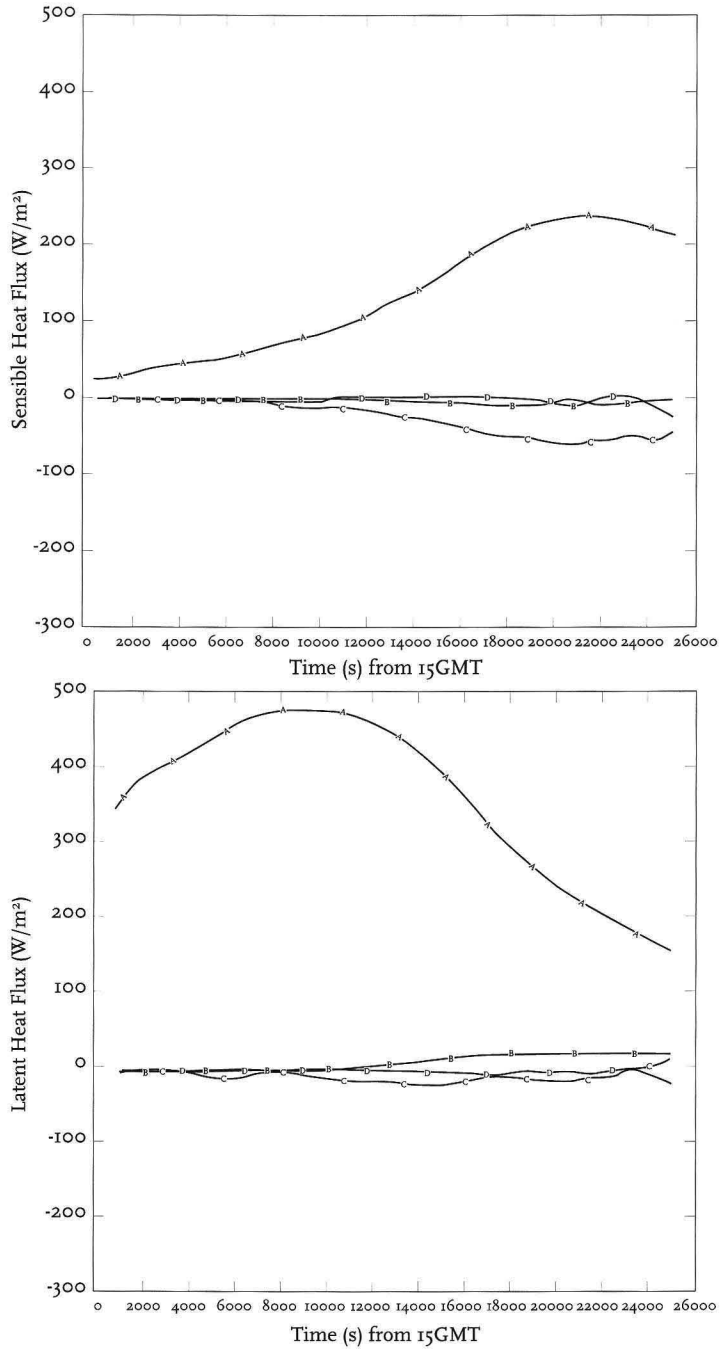
169

Fig. 7. a: (top) Domain-averaged contribution to surface sensible heat (W m^{-2}) versus time from 15 GMT due to A) control simulation, B) variable vegetation, C) clouds, D) interaction of clouds and variable vegetation. b: (bottom) Same as 1 except for latent heat (W m^{-2}).
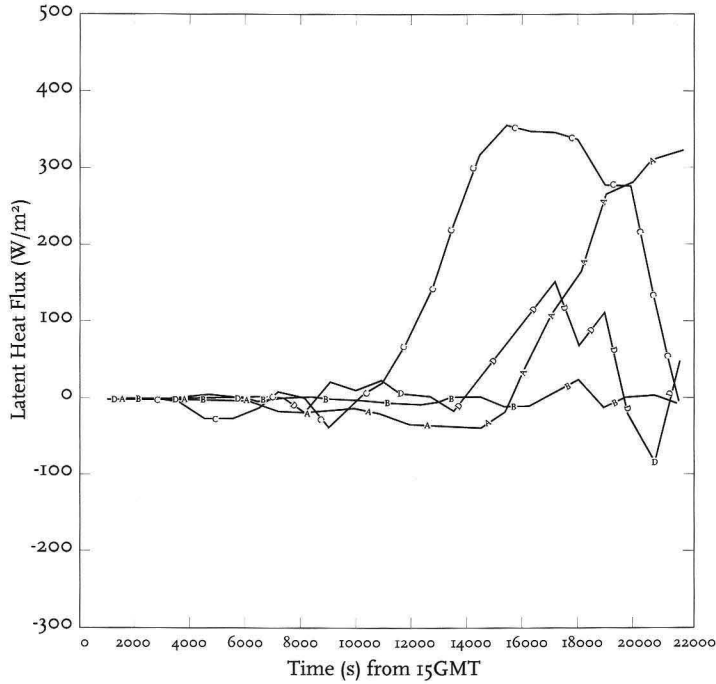
170

Fig. 8. Same as Figure 7b except at 1100 m above ground level.

to variable vegetation alone is minimal over this area. In general, the FIFE study area is fairly homogeneous and could explain the relative lack of contribution due to the variable vegetation. This would also offer support to the conclusion that a linear sum of the patches could be used over the FIFE domain in order to evaluate the total domain averaged fluxes (Sellers et al., 1992). Additional detail on this study are provided in Eastman et al. (1997).

5   Development of mesoscale fluxes

5.1   Parameterization of landscape effects on sensible and latent fluxes

Mesoscale surface inhomogeneity can generate mesoscale circulations in the boundary layer which affect both surface fluxes and fluxes in (and even above) the boundary layer (Pielke et al., 1991; Zeng and Pielke, 1995a) as discussed in the previous sections. It is demonstrated (Zeng and Pielke, 1995b) that these mesoscale fluxes are insensitive to small perturbations in initial and surface boundary conditions as well as model parameters, and hence are parameterizable. Preliminary parameterization schemes have also been developed for turbulent and mesoscale fluxes (Lynn et al., 1995; Zeng and Pielke, 1995a).

171

The turbulent, mesoscale, and total (i.e., turbulent + mesoscale) fluxes within and above the boundary layer are parameterized as a function of five dimensionless variables (Zeng and Pielke, 1995a): the dimensionless height (ζ), the aspect ratio of vertical versus horizontal scales (α), the bulk Richardson number (R_b) (which approximately represents the ratio of the buoyant production/consumption over the wind shear production of the turbulent kinetic energy), the ratio of the eddy turnover time in the boundary layer over the advection time (λ_1), and the ratio of the kinetic energy of the large-scale flow over the horizontal pressure gradient which results from the horizontal differential heating (λ_2). These parameters originated from the concepts of the linear model result and mesoscale potential energy discussed in Section 2.

As an example, Fig. 9 shows the mesoscale sensible heat flux results that are generated from 44 two-dimensional numerical simulations with different synoptic wind and horizontal scales. The mesoscale sensible heat flux is zero at the surface, because the mesoscale vertical velocity is zero. It reaches its maximum value in the middle of the boundary layer, and becomes negative at the top of the boundary layer (Fig. 9a). It is also negative above boundary layer (figure not shown) due to the mesoscale return flow there. Large errors would occur if a polynomial as a function of height alone is used for the parameterization, as shown in Figures 9a and 9b. Using additional dimensionless variables, however, provides significantly better fits in Fig. 9c.

It needs to be emphasized that the flux itself is directly parameterized as a function of dimensionless variables (Zeng and Pielke, 1995a). In contrast, most of the conventional turbulence parameterization schemes assume various functional forms for the turbulent diffusivity, and obtain the turbulent (sensible heat) flux as this diffusivity multiplied by the vertical gradient of potential temperature. In the convective boundary layer, even though the mesoscale and turbulent sensible heat fluxes have different vertical profiles, the total flux is a quasi-linear function of height even over a heterogeneous surface, just like that over homogeneous terrain, because potential temperature is well mixed due to turbulent and mesoscale processes. More generally, when moist processes (e.g., the mesoscale downdraft associated with deep convection) are considered in boundary layer parameterizations, the direct parameterization of flux (rather than the diffusivity) is also expected to be a better approach.

For a specific flux, 15 to 21 coefficients are used (Zeng and Pielke, 1995a). The approach to obtain horizontal scales and the maximum horizontal temperature difference within a large-scale model grid box has not yet been developed. Therefore, simplification of the latter parameterizations is required for its implementation in large-scale models.

In addition to mesoscale fluxes in the boundary layer, mesoscale circulations introduce inhomogeneity in the wind, temperature, and humidity fields at the first model level above ground in a model. Therefore, the current practice of assuming the same near-surface variables in computing surface fluxes over heterogeneous terrain is questionable. Furthermore, mesoscale circulations are important for the triggering of convection. These are issues that
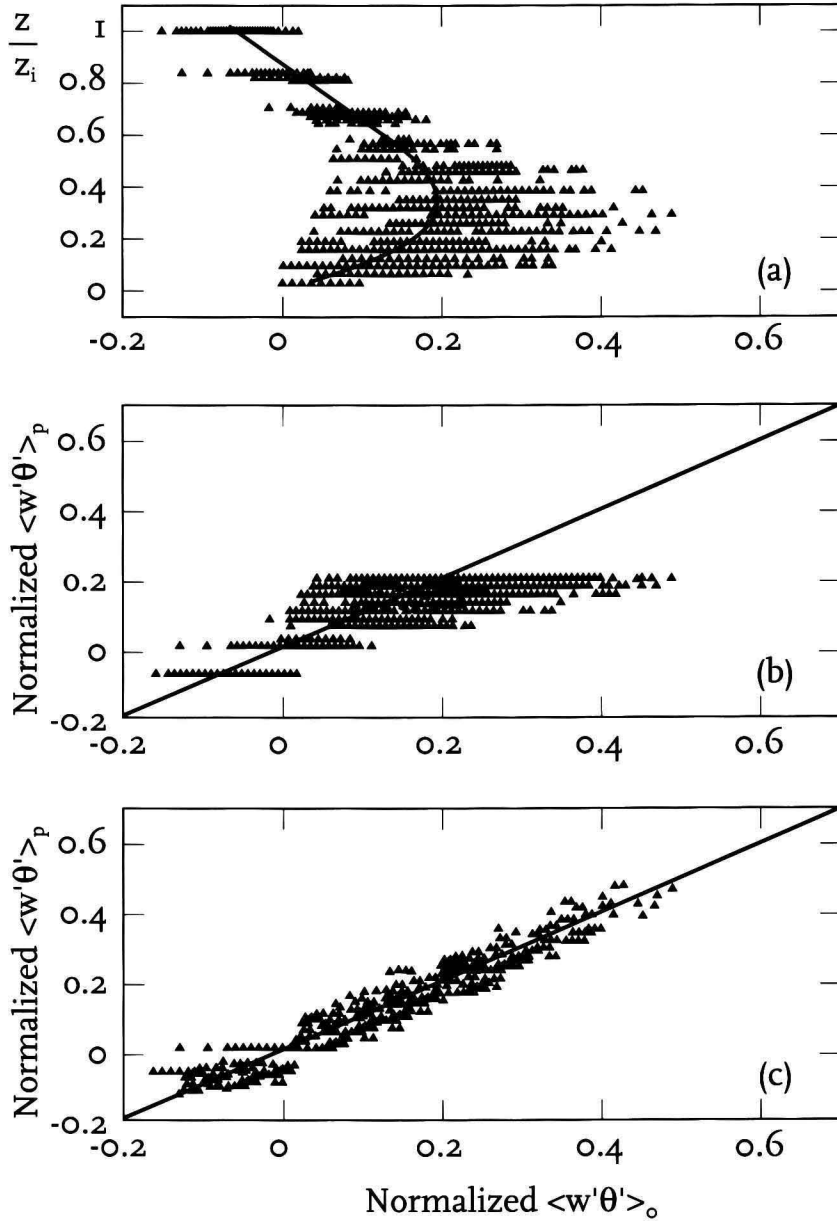
Fig. 9. The dimensionless mesoscale sensible heat flux in the boundary layer obtained from mesoscale numerical simulations, denoted by the subscript o, versus the dimensionless height in (a), versus that obtained from the fitted polynomial of dimensionless height alone in (b), and versus that estimated from our parameterization scheme using four dimensionless variables in (c), denoted by the subscript p. In (a), the solid line represents the best fitted polynomial of height alone.

need to be studied in subsequent research.

5.2 *Validation of parameterization*

The direct verification of model results of mesoscale fluxes is difficult. For aircraft observations, systematic and random errors exist between time- (or space-) averaged fluxes from aircraft, and the ensemble averages which are actually used in numerical models. Specifically, the systematic and random errors can be defined as

$$S \;=\; (F_c - F_e)/F_c \quad, and \quad R = \sigma_F/F_c \,, \tag{13}$$

where F_e is the the ensemble average flux, and F_c is the aircraft-observed flux with a flight leg L, and σ_F is the standard deviation of F_c. In the convective boundary layer, S and R are linked to L and the boundary layer height z_i as (Lenschow et al., 1994):

$$L/z_i \;\sim\; \frac{2.2}{S} \left(\frac{z}{z_i}\right)^{1/2} \quad, and \quad R \;\sim\; 1.16 \left(\frac{z}{z_i}\right)^{1/6} \left(\frac{z_i}{L}\right)^{1/2} . \tag{14}$$

Near the surface, for a typical leg of $L = 5\ z_i$, both S and R are quite small so that aircraft observations can accurately represent ensemble averages. However, turbulent fluxes are dominant near surface. Near the top of the boundary layer, mesoscale fluxes are dominant; however, for a typical leg of $L = 5\ z_i$ at a height of $z = 0.8\ z_i$, S and R are quite large (i.e., 39% and 50%, respectively). Alternatively, limiting S and R to 10% would require L to be $20\ z_i$ and $125 z_i$, respectively. In the middle of the convective boundary layer, mesoscale and turbulent fluxes are similar in magnitude, and this might be the best altitude for aircraft verification of mesoscale fluxes. However, it is still difficult to distinguish between mesoscale spatially-coherent fluxes and mesoscale temporally-transient fluxes.

6 Conclusions

Among the major conclusions from our analytic study are:

(1) With little or no synoptic wind over heterogeneously heated landscape patches, the mesoscale vertical velocity is in phase with the convective boundary layer (CBL) temperature perturbations and the mesoscale heat flux is positive and of the same order as the diabatic heat flux within the

174

CBL. Above the CBL, the mesoscale heat flux is negative and penetrates into the free atmosphere through a depth comparable to the depth of the CBL.

(2) In the presence of synoptic flow, the mesoscale perturbation is in the form of propagating waves that penetrate deeply into the free atmosphere. As a result, there is a net downward flux of momentum, which is dissipated within the CBL by turbulence. Mixing with the environment of the air particles displaced by the waves results in a net negative mesoscale heat flux, which contributes to the weakening of the stability of the free atmosphere.

(3) Strong synoptic advection can significantly reduce the horizontal temperature gradients in the CBL, thereby weakening the intensity of the mesoscale flow. Turbulent diffusion also weakens the temperature gradients and the intensity of the mesoscale flow when the horizontal wavelength of the surface heat patches is comparable to the CBL depth.

(4) When the synoptic wind is very strong, the mesoscale perturbation is very weak and vertically trapped.

Among the major conclusions from our numerical modeling tools are:

(1) The important controls on mesoscale fluxes resulting from land surface heterogeneities include boundary layer depth, horizontal size of the surface heat patches, the potential temperature difference between the different patches, the surface sensible, moisture, and momentum fluxes, and the height above the surface (Zeng and Pielke, 1995b).

(2) Knowledge of the details of the landscape (including soil moisture, landscape type, and fractional coverage) are essential for accurate simulations of mesoscale and cumulus processes over land during the summer (Shaw, 1995; Shaw et al., 1997; Pielke et al., 1998).

Among the conclusions from our observational analyses are:

(1) There are significant spatial variations in surface heat and moisture fluxes due to landscape variations. Often these variations in the middle of a summer or spring day are hundreds of W m^{-2}.

(2) These variations are evident above the surface as well, however, we still do not have definitive observational evidence of mesoscale fluxes due to landscape variations.

Future work is needed to confirm or refute our modeling-based conclusions using observational data. If confirmed, a general parameterization of mesoscale effects due to convective boundary layer development over spatially-varying landscapes needs to be implemented.

Acknowledgments